ADVANCED FUNCTIONAL MATERIALS
www.afm-journal.de

Ultrafast Electron Dynamics at the P-rich Indium Phosphide/TiO_2 Interface

*Jonathan Diederich, Jennifer Velazquez Rojas, Agnieszka Paszuk, Mohammad Amin Zare Pour, Christian Höhn, Isaac Azahel Ruiz Alvarado, Klaus Schwarzburg, David Ostheimer, Rainer Eichberger, Wolf Gero Schmidt, Thomas Hannappel, Roel van de Krol, and Dennis Friedrich**

The current efficiency records for generating green hydrogen via solar water splitting are held by indium phosphide (InP)-based photo-absorbers, protected by TiO_2 layers grown through atomic layer deposition (ALD). InP is also a leading material for photonic integrated circuits and computing, where ultrafast near-surface behavior is key. A previous study described electronic pathways at the phosphorus-rich (P-rich) surface of p-doped InP(100) using time-resolved two-photon photoemission (tr-2PPE) spectroscopy. Here, the intricate electron pathways of the P-rich InP surface modified with ALD-deposited TiO_2 are explored. Photoexcited bulk InP electrons migrate through a bulk-to-surface transition cluster of states and surface states and inject into the TiO_2 conduction band (CB). Energy levels and occupation dynamics of CB states in P-rich InP and TiO_2 adlayers are observed, with discrete states preserved up to 10 nm TiO_2 deposition. Thermalization lifetimes of excited electrons > 0.8 eV above the InP conduction band minimum (CBM) are preserved for layer thicknesses up to 2.5 nm. Annealing at 300 °C to achieve crystalline TiO_2 reconstructions destroys interfacial states, affecting charge transfer. These observations enable innovative engineering of the P-rich InP/TiO_2 heterointerface, opening new possibilities for studying hot-carrier extraction, adsorbate effects, surface plasmons, and improving photovoltaic and PEC water-splitting devices.

1. Introduction

Hydrogen obtained from renewable sources is crucial for the transition toward a more sustainable energy landscape. The direct conversion of water into hydrogen via photoelectrochemical (PEC) devices may provide an effective alternative to traditional photovoltaic (PV)-electrolyzer configurations, with the advantage of decreased current densities and effective cooling of the absorbers.[1] The highest solar-to-hydrogen efficiencies achieved to date utilize III-V semiconductor photoabsorbers,[2,3] thanks to their advantageous combination of direct bandgaps, high electron mobilities as well as good bandgap and surface tunability.

Our detailed examination focuses on the surface of p-doped (zinc) indium phosphide (p-InP), chosen for its well-studied surface structure and its record-setting performance as a photoelectrode for PEC devices, which serves as a benchmark in the field.[3–9] In addition, InP is also a key material in photonic integrated circuits due to its excellent optoelectronic properties.[10–12] A direct bandgap of 1.344 eV at room temperature[13] allows for highly efficient light emission and -absorption, required for on-chip lasers and photodetectors. The high electron mobility of InP facilitates fast carrier transport in high-speed photonic devices.[13] State-of-the-art photonic integrated circuits have moved to the use of InP membranes of sub-µm thickness on Si.[12] As InP is compatible with

J. Diederich, J. V. Rojas, C. Höhn, K. Schwarzburg, R. Eichberger, R. van de Krol, D. Friedrich
Institute for Solar Fuels
Helmholtz-Zentrum Berlin für Materialien und Energie GmbH
14109 Berlin, Germany
E-mail: friedrich@helmholtz-berlin.de

The ORCID identification number(s) for the author(s) of this article can be found under https://doi.org/10.1002/adfm.202409455

DOI: 10.1002/adfm.202409455

J. Diederich, R. van de Krol
Institut für Chemie
Technische Universität Berlin
10623 Berlin, Germany

A. Paszuk, M. A. Z. Pour, D. Ostheimer, R. Eichberger, T. Hannappel
Institut für Physik
Technische Universität Ilmenau
98693 Ilmenau, Germany

I. A. R. Alvarado, W. G. Schmidt
Lehrstuhl für Theoretische Materialphysik
Universität Paderborn
33095 Paderborn, Germany

high-speed modulation formats such as PAM-4 and coherent communication,[11] this allows for the high-performance optoelectronic properties of InP to be combined with cost-effective, mature Si electronics.[11,12] InP and III-V growth directly on Si is also an area of active research, including by some of the present authors.[14,15] 193 nm optical nanolithography processes have been applied to InP-Membrane-on-Silicon circuits, making the technology compatible with existing, scalable production processes.[11,16]

InP(100) is used as the standard substrate cut for InP membranes in photonic integrated circuits.[11,17,18]

Photonic integrated devices using InP membranes can reach data rates of the order of hundreds of GHz, aiming to reach the THz range.[11] This corresponds to the picosecond timescale and below, relying on the rapid relaxation and recombination times in InP to allow for fast switching and modulation.

Understanding electron behavior near the InP(100) surface on the sub-ps timescale is key to further pushing the data rates used, and being able to model behavior of InP-based photonics for, e.g., next-generation 6G and 7G cellular communication.[11] Other applications of InP include photonic computing, and optoelectronic sensors used in biomedical monitoring or industrial manufacturing.[11,16] With femtosecond lasers becoming more common for, e.g., surgeries,[19] understanding sensor behavior on these timescales is then required.

Several distinct surface reconstructions are known for InP(100), with different electronic energy levels, lifetimes, stability, and overall performance.[20–23] In a hydrogen-containing reducing atmosphere, such as an metalorganic vapor phase epitaxy (MOVPE) reactor, typically two surface reconstructions are possible: i) a phosphorus-terminated (P-rich) p(2 × 2)/c(4 × 2)-reconstructed surface, which consists of buckled P dimers stabilized by one H atom each,[24,25] and ii) a (2 × 4) (In-rich) mixed dimer surface, which is terminated by a mixed dimer formed by In and P atoms.[26,27] Which surface reconstruction is observed depends on the phosphorus chemical potential for a given molar flow of the phosphorus precursor, as well as on the surface temperature. Previous studies concentrated on the In-rich surface reconstruction on n-doped InP. Although the P-rich, p-doped InP surface has been investigated, no electronic surface states could be identified within the experimental precision and UHV-handling procedure of these studies.[28–30] The P-rich, p-doped InP(100) (p-InP) surface thus remains less well understood.[22,25,29] In a recent paper[31] we were able to for the first time experimentally probe the electron dynamics at this P-rich, p-doped InP surface, finding evidence of a detailed band structure consisting of a valence band state near the valence band maximum (VBM), a surface state pinning the Fermi level, six distinct conduction band surface resonances as well as a cluster of states in the near-surface region, serving as a bulk-to-surface transition for photoexcited bulk electrons.

Most III-V semiconductor surfaces, including InP(100), are susceptible to the formation of native oxide layers or dissolution of the surface under the aqueous conditions found in a PEC cell.[32,33] The use of oxide materials as protective layers can mitigate this issue due to their superior electrochemical stability.[5,34–38] These protective layers can also serve as selective contacts and thereby facilitate the efficient transport of photoexcited charge carriers from the semiconductor surface to the oxide/electrolyte interface, and display superior PEC performance compared to the untreated semiconductor surface.[5,35,36,39–41] To increase stability beyond the limits of the native P- and In-oxides, Lee et al. added a TiO_2 surface layer with atomic layer deposition (ALD), showing good PEC performance for 2–5 nm TiO_2 deposited onto structured InP surfaces.[7]

Among various oxide materials, TiO_2 stands out as a particularly suitable option due to its favorable conduction band alignment with many commonly studied PEC semiconductors.[3,35,40] In 2014, Yin et al. used a 10 nm amorphous TiO_2 layer as an electron-selective contact for p-InP, resulting in a heterojunction solar cell with an efficiency of 19.2%.[3] In 2015, Lin et al. demonstrated the effectiveness of an optically transparent and electron-conducting TiO_2 layer on a p-InP photocathode by achieving a photocurrent onset potential in excess of 800 mV versus the reversible hydrogen electrode (RHE), a new record for p-InP.[5] In 2018 Cheng et al. demonstrated a record solar-to-hydrogen (STH) conversion efficiency of 19% using a TiO_2-protected GaInP/GaInAs dual-junction absorber functionalized with Rh nanoparticles as a catalyst for the hydrogen evolution reaction (HER). Their monolithic tandem device still holds the world record for bias-free solar water splitting with III-V photoelectrodes.[2] Further increases in PEC efficiency will likely involve further study of interfacial electronic properties between semiconductor and oxide layer, as well as band alignment and defect transport.[33] Here a more detailed understanding of electronic pathways both in the InP surface and at the interface to additional functional layers would help more effectively select suitable surface modifications for InP-based photoelectrodes.

TiO_2 layers can transport both electrons and holes through different mechanisms. Electrons photoexcited in a p-type (photocathode) semiconductor migrate from the semiconductor conduction band into the TiO_2 conduction band, facilitated by their favorable band alignment, and subsequently via the HER catalyst into the electrolyte.[2,5,42] TiO_2 can also conduct holes via bulk defect states in the bandgap, an effect that has been used for the protection of III-V and silicon photoanodes with chemically inert and optically transparent TiO_2 protection layers.[34,43,44] This phenomenon of hole-conducting "leaky" TiO_2 is actually detrimental for p-type photocathodes, as the transport of holes (majority carriers) to the surface increases recombination and consequently leads to both photovoltage and photocurrent losses.[5,41] Lin et al.[5] demonstrated better photocurrent onset potentials with defect-free TiO_2 compared to leaky TiO_2 on p-InP, related to favorable band alignment with a large valence band offset, resulting in low recombination rates and the creation of an electron-selective contact.

In a previous study we explored the surface- and sub-surface electronic states on the P-terminated InP(100) surface,[31] prepared using MOVPE. Our current study investigates the effects of modification of this surface by depositing TiO_2 protection layers using ALD[45] and tracks the electron pathways in the emerging TiO_2 states with femtosecond resolution. Information on surface composition is obtained using X-ray and ultraviolet photoelectron spectroscopy (XPS, UPS), reflection anisotropy spectroscopy (RAS), low-energy electron diffraction (LEED), and atomic-force microscopy (AFM) imaging. We utilize time-resolved two-photon photoemission (tr-2PPE) to probe unoccupied conduction band

states and analyze electron dynamics in both the TiO_2 layer and the underlying InP bulk and surface. This allows us to assess conduction band alignment, the likelihood of electron transfer between the layers, and modifications to surface states resulting from interactions with deposited materials. TiO_2 layers of increasing thicknesses are studied, enabling the observation of both InP bulk and TiO_2 surface features until the TiO_2 layer thickness exceeds the information depth of tr-2PPE. By stepwise passivation of the InP surface, we gain insights into whether electronic states are associated with surface or bulk features and through which pathway the electrons diffuse into the TiO_2 layer.[5] Given the presence of at least nine distinct near-surface states on the P-rich InP surface as previously reported,[31] this interface presents a background on which the effects of adlayers and adsorbates may be tested. As inelastic mean free paths for electrons in tr-2PPE are in the nm range,[46] it is possible to observe the states at the P-rich InP/TiO_2 interface up to a depth of several nm. This allows us to present a detailed experimental view of this interface below the semiconductors surface, and revealed further details about the sub-ps relaxation of carriers in InP.

2. Results

2.1. Surface Modification through Tio_2 Deposition

The distinct surface states observed on the P-rich InP surface [31] serve as an ideal and sensitive probe for monitoring surface modifications through TiO_2 deposition in the ALD process. The changes in electron energetics and dynamics were studied as a function of TiO_2 layer thickness. Tracking the deposition of TiO_2 on the pristine P-rich InP surface is achieved through tr-2PPE and XPS. Depositing TiO_2 onto III-V semiconductors is known to create a type II p-n heterojunction.[5] Previous studies on surface-passivated GaP(100), which shares a similar zincblende structure with InP(100), have shown that an increasing thickness of an n-type TiO_2 layer enhances the depletion layer in the InP semiconductor, thereby improving photo-induced charge separation.[34,47–49]

High-resolution XP spectra as well as a detailed discussion of the results can be found in Figures S7 and S8, and Note S1 (Supporting Information), with key points repeated here. Prior to TiO_2 deposition, only small O 1s and C 1s signals are visible, most likely due to adsorbates from exposure to ambient air during transfer of the sample from the MOVPE reactor to a UHV-chamber. With increasing number of ALD cycles, XPS results (Figures S7 and S8, Supporting Information) show the formation of characteristic TiO_2 peaks, O KLL, O 1s and Ti 2p, indicating the progressive formation of TiO_2 on the InP(100) substrate. Additional peaks related to phosphate and phosphite bonds at the InP/TiO_2 heterointerface may also be observed, particularly $InPO_4$ and $In(PO_3)_3$, with no evidence for In_2O_3.[50] The Ti ($2p_{3/2}$) and Ti ($2p_{1/2}$) core-level peaks at 459.0 and 464.7 eV show the expected 2:1 ratio and indicate the presence of Ti^{4+} cations; we did not observe any peaks corresponding to Ti^{3+} defects.[51] AFM measurements (Figure S2, Supporting Information) indicate complete surface coverage already at a 2.5 nm TiO_2 thickness.

Figure 1 shows tr-2PPE measurements on the InP / TiO_2 surfaces using 533 nm VIS pump and 276 nm UV probe beams (VIS – UV), displayed in a pseudo-3D transient plot. Emission energies are given versus vacuum level, to obtain energies versus Fermi level one may add the work function of the respective surfaces to this (Figure S10, Supporting Information). The P-rich InP(100) surface prior to TiO_2 deposition is depicted in (a-c), a detailed analysis of this surface was performed in a previous paper.[31] A total of at least nine distinct states are observed in the near-surface region on P-rich InP: six distinct conduction band states C1 – C6, a dense cluster of states ≈1.6 eV above the CBM (between C5 and C6) that increases the bulk-to-surface transition rates of photoexcited bulk electrons, a valence band state V1, as well as a surface state within the bandgap that pins the Fermi level around the mid-gap position.[22,25,31] Several additional conduction band states were suspected from composite Voigt-fitting of data and visual inspection, but could not be identified conclusively. Electronic charge held in the surface state and surface resonances was found to cause a potential barrier to emission of electrons, resulting in vacuum states.[52,53] This manifests as a cut-off in emission at ≈0.23 eV as observed in Figure 1a–c, which varies by ≈0.1 eV depending on pump- and probe intensities in tr-2PPE, as this changes the density of photoexcited carriers.

After deposition of TiO_2 on the P-rich InP surface, there still appear to be vacuum state-related cut-offs of the emission, with the cut-off shifted to higher kinetic energy. Adsorption or deposition of material onto the InP surface is likely to change the dielectric properties of the surface, and therefore to affect vacuum states and surface Fermi level pinning, which may change the sample work function.[54] Interestingly, for all TiO_2 thicknesses of the spectra in Figure 1, emission is visible below the cut-off, with an amplitude of ≈20% that of the amplitude above the cut-off, and decreasing with distance from the cut-off energy. This observation was also made by Onda et al.[52] on rutile (110) TiO_2 surfaces, which they theorized to be due to surface inhomogeneity leading to slightly varying work functions in different regions. Whilst on the bare P-rich InP(100) surface the cut-off position is the same for UV – UV and VIS – UV, after TiO_2 deposition the cut-offs differ between UV- and VIS pumping. In the measurements given in Figure 1, kinetic energy cut-offs were found for 1.3 nm TiO_2 at 0.73 eV in VIS – UV (Figure 1e) and 1.06 eV in UV – UV (Figure 1f); for 2.5 nm TiO_2 at 0.66 eV in VIS – UV (Figure 1h), and at 0.91 eV in UV – UV (Figure 1i); and for 10 nm TiO_2 at 0.43 eV in VIS – UV (Figure 1k) and 0.91 eV in UV – UV (Figure 1l). Two clear trends are noticeable: First the cut-off energies increase after initial TiO_2 deposition, which may be explained by a higher density of surface states available on the deposited TiO_2 layers than on the P-rich InP surface. Alternatively, band bending at the P-rich, p-doped InP surface may also be increased by deposition of an n-doped TiO_2 adlayer, increasing the occupancy of surface states and therefore cut-off energies. The other trend is an increased divergence in emission cut-offs between UV – and VIS – pumping after initial TiO_2 deposition, as well as when moving to a 10 nm TiO_2 layer thickness. This indicates differences in the effectiveness of populating surface states via the UV and VIS beams, likely in part caused by the much higher absorptivity of TiO_2 in the UV – compared to the VIS – wavelength range.[13,55] The UV beam photon energy of 4.49 eV considerably exceeds literature values for the TiO_2 bandgap of 3.0-3.2 eV,[52,56–60] and should therefore access TiO_2

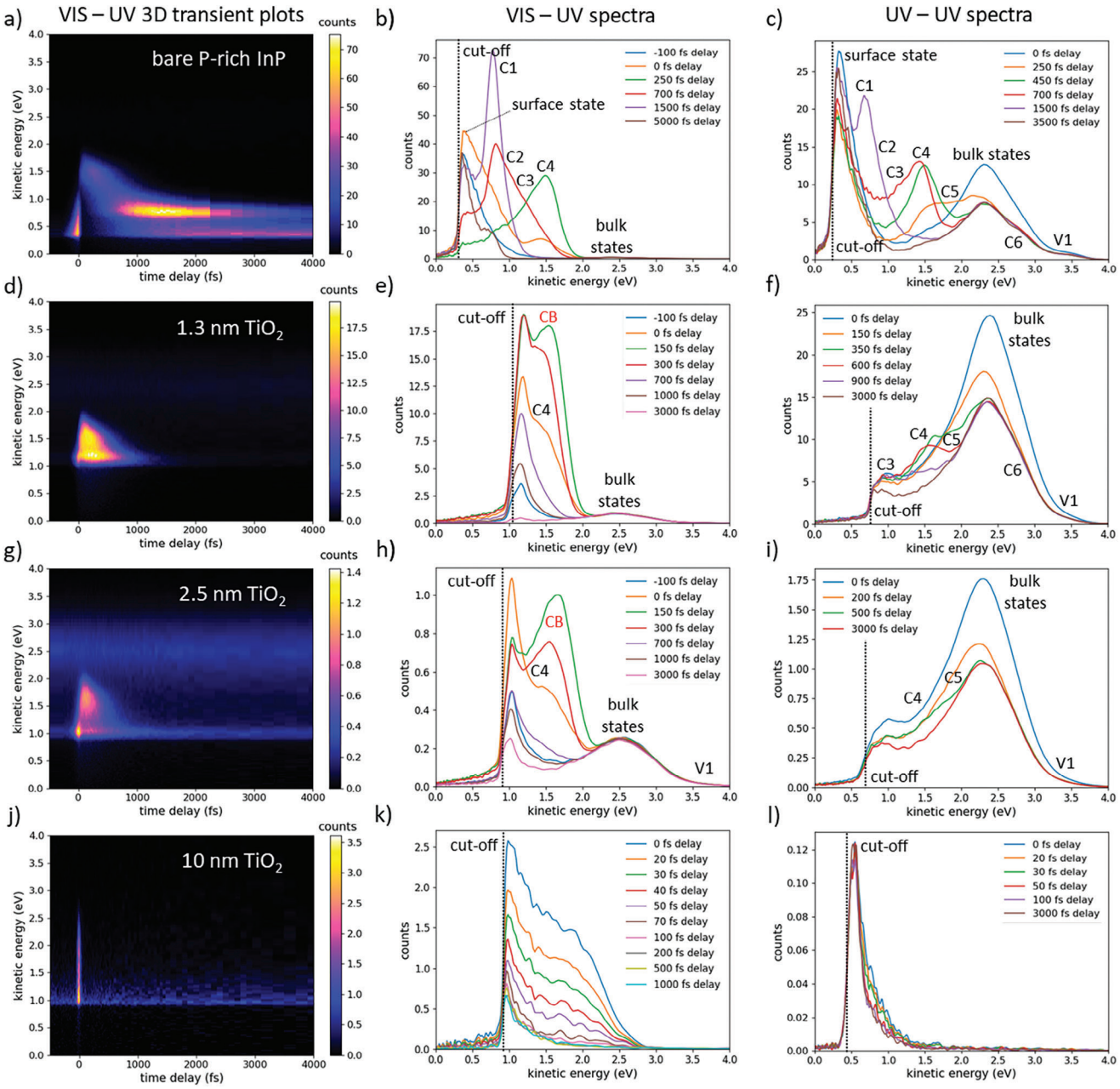

Figure 1. tr-2PPE measurements at the P-rich InP surface, prior to and after deposition of TiO_2 layers of increasing thickness. The left column shows VIS – UV 3D transients, the middle column the corresponding VIS – UV spectra, and the right column shows spectra in UV – UV. The top row a–c) shows the P-rich p-InP surface, the second row d–f) after deposition of 1.3 nm TiO_2, the third row g–i) with 2.5 nm TiO_2, and the bottom row j–l) after 10 nm TiO_2 deposition. States observed on the P-rich InP surface are denoted, those that were found after TiO_2 deposition are also given, as well as a potential additional conduction band (CB) state clearly visible in (f) and (i). The "bulk states" denote a cluster of states in the near-surface region, serving as a bulk-to-surface transition for bulk electrons.

conduction band states, which VIS photons at ≈2.33 eV cannot. This implies that the transfer of electrons photoexcited in the InP bulk to the TiO_2 surface must be efficient, or the pump power increase from UV to VIS would not yield an increase in surface charging across all layer thicknesses observed.[52,56–60] As the UV photons can directly access TiO_2 states, this leads to changes in cut-off with TiO_2 thickness, whereas the VIS cut-off is stable after initial deposition. Possibly, the density of defect states in TiO_2 may also decrease as layer thickness increases, whilst not affecting VIS pumping from the InP layer. Reference air mass 1.5 spectra for solar irradiation show the highest spectral irradiance at 450–490 nm, with a sharp drop-off below ≈440 nm, as well as a gradual decrease toward longer wavelengths.[61] The majority of irradiance then occurs at photon energies lower than the TiO_2 bandgap, likely correlating to photoexcitation pathways more similar to the VIS-pump used here, rather than the

UV pulses.[52,56–61] This would allow for a significant fraction of absorption to occur in the InP photoabsorber as intended. The fraction of photons transmitted through a layer of thickness d can be estimated as

$$T = 10^{-\alpha \cdot d} \quad (1)$$

where T is the transmitted fraction of photons, and α the absorption coefficient. A detailed calculation is given in Note S2 (Supporting Information), with 98% of VIS light transmitted through TiO_2 layers up to 10 nm in thickness, whilst UV transmission is ≈81% at 1.3 nm, 67% at 2.5 nm, and only 20% at 10 nm TiO_2 thickness.

This interpretation of emission cut-off, reliant on the density of photoexcited carriers, is further supported by the dependence of cut-offs on excitation intensity after TiO_2 deposition. For instance, with a 1.3 nm TiO_2 layer, reducing VIS power from 1.0 to 0.5 mW led to a decrease in cut-off from 1.06 to 0.96 eV in energetic position. This power dependence is consistent across various thicknesses of TiO_2 layers. Onda et al. have also reported differences in work functions obtained from 2PPE versus XPS emission of 0.2 – 0.3 eV in rutile TiO_2, attributed to power-dependent surface charging.[52] Due to the energetic cut-off, it remains uncertain whether the mid-gap surface state observed on the bare P-rich InP(100) surface, which pins the Fermi level, persists after TiO_2 deposition. However, given that this surface state is commonly associated with P-dangling bonds in the literature,[22,24,25] it is highly probable that it is no longer present following the deposition of an oxide such as TiO_2.

At a thickness of 1.3 nm TiO_2, the sample's work function (Φ), determined from XPS analysis (Figure S10, Supporting Information), is measured at 5.89 eV. This value can be utilized to determine the position of the Fermi level E_F (vs vacuum) from the position of the signal cut-off Evac using the equation:

$$E_{vac} - E_F = \Phi \quad (2)$$

Given the cut-offs observed at 0.73 and 1.06 eV in VIS – UV and UV – UV (Figure 1e,f), the surface Fermi level of the sample lies between −4.83 and −5.16 eV relative to vacuum, or 0.02 and 0.35 eV above the InP VBM. This alignment is consistent with the expected Fermi level position in bulk p-type InP, which should be ≈0.04 eV above the VBM in our sample.[22] However, it contradicts the previous position of the surface state, which pinned the Fermi level at 0.5 – 0.6 eV above the VBM, indicating that the surface pinning of the Fermi level has indeed been disrupted following TiO_2 deposition.

This is in agreement with our DFT calculations for the initial stage of InP surface oxidation. Adsorption of single water molecules on the ideal P-rich InP(001):H surface,[20] considered the initial step of the surface oxidation, essentially maintains the surface electronic states characteristic of the clean surface (Figure S11a,c, Supporting Information). The Fermi level pinning observed on P-rich InP(001):H surfaces is associated with P dangling bonds exposed upon hydrogen desorption,[22,25] generating a relatively flat, half-occupied band within the InP bulk bandgap (Figure S11b, Supporting Information). Adsorption of hydrogen or hydroxyl groups resulting from dissociative water adsorption passivates the P dangling bond defect, restoring flat band conditions (Figure S11d, Supporting Information).

The electronic states observed in the near-surface region of bare P-rich InP (Figure 1a–c) are visually retained after TiO_2 deposition at 1.3 nm (Figure 1d–f) and 2.5 nm (Figure 1g–i) and may be fitted using composite Voigt-fitting. After TiO_2 deposition, surface resonances in UV – UV exhibit reduced amplitude relative to the surface-to-bulk transition cluster of states (Figures 1 and 2). As the absorbed power per atomic layer decreases exponentially with depth, relocating localized surface resonances from the sample surface to 1.3 or 2.5 nm into the material following TiO_2 deposition significantly diminishes their emission proportion. However, the bulk-to-surface cluster of states on P-rich InP, consisting of energetically aligned states across several atomic layers,[31] experiences a relatively smaller reduction in emission compared to pure surface resonances. Conversely, emission using VIS – UV does not exhibit a clear suppression of pure surface resonances, with pumped conduction band states remaining prominent compared to bulk-to-surface transition peaks. This disparity is attributed to reduced absorption of the VIS pump within the deposited TiO_2 layer, increasing the relative emission from P-rich InP surface resonances. The InP valence band edge signal is strongly suppressed in amplitude after TiO_2 deposition in both VIS – UV and UV – UV, in agreement with HE I UPS data (Figure S9, Supporting Information).

Due to the limited visual clarity of peaks in UV – UV after deposition, further data processing is performed. To highlight the time-dependent component of emissions, the steady-state emission is subtracted. The background of steady-state emission is calculated by summing emissions from 3000 to 6000 fs delay time, where time-dependent emission has decayed across all samples. Subtracting the steady-state emission is particularly helpful for the UV – UV data, where time-dependent emission is smaller relative to time-independent emission as compared to VIS – UV emission. The time-dependent emission in UV – UV for the P-rich InP surface, as well as after deposition of 1.3 and 2.5 nm TiO_2, is given in **Figure 2**a–c respectively. In (b) and (c), the number of displayed delay slices has been increased to illustrate more detailed temporal development.

On the P-rich InP surface (Figure 2a), we observe time-dependent emission peaks associated with surface conduction band resonances C1-6, a bulk-to-surface transition cluster of states (bulk states) and V1.[31] The V1 state is weakly observed at t = 0 fs, indicating predominantly time-independent emission from this state. Although the surface state pinning the Fermi level is present ≈0.4 eV, it does not manifest as a distinct peak as it is cut-off. Additionally, there are suspected states at ≈1.0, 1.65, and 2.1 ± 0.1 eV, which were not reliably identifiable previously.[31] The positions of these states on the bare P-rich InP surface are given in Table S3 (Supporting Information), along with their positions after TiO_2 deposition. For a comprehensive interpretation of the P-rich InP surface.[31]

As observed in Figure 1, conduction band states are notably suppressed in amplitude relative to the bulk-to surface transition in UV – UV after TiO_2 deposition, a trend which persists in the time-dependent components of emission in Figure 2b,c. Peaks exhibiting stability across delay times are discernible at energetic positions corresponding, within uncertainty, to the surface states

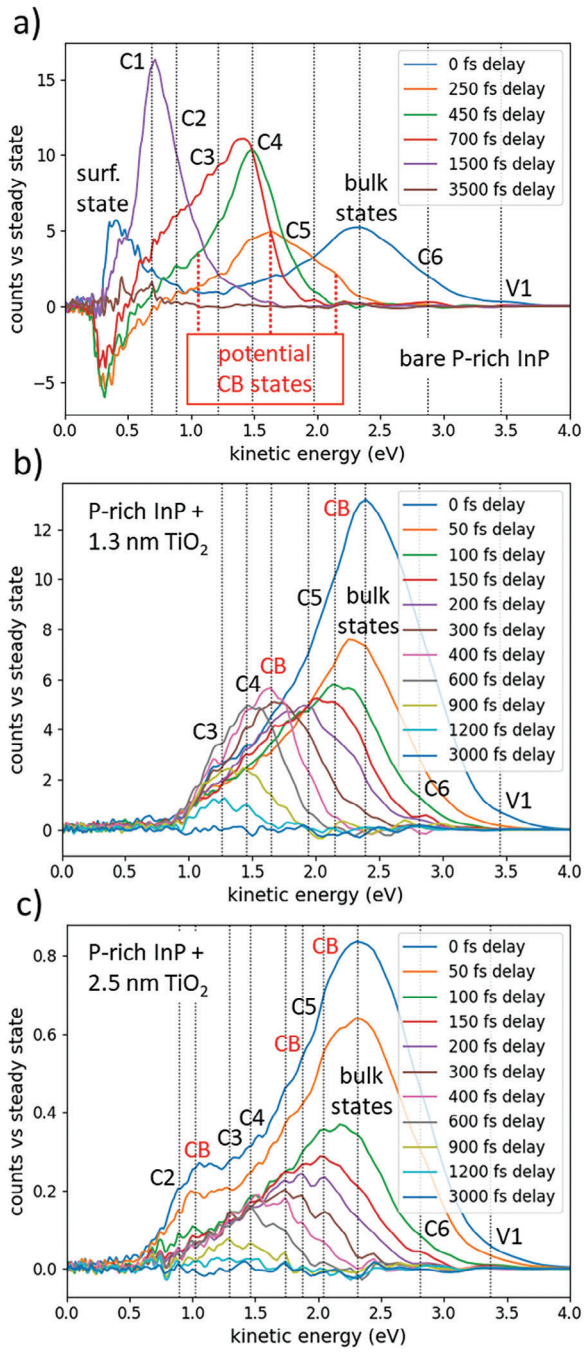

Figure 2. Time-dependent component of UV – UV emission for the bare P-rich InP(100) surface in a), and after 1.3 nm b) and 2.5 nm TiO_2 deposition c), raw data in Figure 1c,f,i). P-rich InP surface states C1-6 as well as the bulk-to-surface cluster ("bulk states") are denoted. Suspected CB states on the bare surface are given, and denoted were observed after TiO_2 deposition.

on the bare P-rich InP surface, as illustrated in Figure 2, with exact positions detailed in Table S3 (Supporting Information). This indicates that P-rich InP surface states, predominantly associated with surface P-dimers on the bare P-rich InP(100) surface, remain intact even after oxidation at the InP/P-oxide/TiO_2 interface. Due to the vacuum state-related cut-off, no states below C3 are visible at 1.3 nm TiO_2 in Figure 2b, while states below C2 are cut-off 2.5 nm in Figure 2c. However, since InP C1 is related to both bulk and surface features as previously described,[31] we expect it is still present at the P-rich InP/TiO_2 interface, especially as the other conduction band surface resonances of P-rich InP appear to be preserved. Composite Voigt fitting weakly indicate a state below the cut-off energy at both 1.3 and 2.5 nm TiO_2, located energetically around the position of C1 on the bare P-rich InP(100) surface.

The peaks exhibit less distinctiveness compared to previous observations, with kinetic energies displaying a roughly gaussian distribution. As previously demonstrated, at TiO_2 thicknesses of 1.3 and 2.5 nm, the majority of both UV and VIS photons pass through the TiO_2 layer, indicating that the majority of photoexcited electrons originate within the InP layer. However, due to the limited escape depth of photoemitted electrons and the higher absorptivity of the UV probe compared to the VIS pump, a greater fraction of emission is expected to occur from the TiO_2 adlayer. At 1.3 nm, peaks are only weakly visible, becoming more distinct at 2.5 nm. Specifically, at 1.3 nm, emission amplitudes increase from the bulk states to C4, while at 2.5 nm, emission decreases as electrons evacuate from the InP bulk-to-surface transition states and halt around C4. The thicker TiO_2 layers may present more potential states for electron transfer from the InP layer and facilitate more efficient extraction of photoexcited carriers, with changes in band alignment potentially contributing to this effect. The persistence of peaks on the bare P-rich InP surface over a range of hundreds of fs delay time implies that photoexcited electrons within the InP bulk continue to cross the P-rich InP / TiO_2 interface, entering the dense manifold of states within the TiO_2 layer and being emitted from there.[52,62] A schematic depiction of this interface is given in Figure S13 (Supporting Information). The dense DOS in the TiO_2 conduction band likely leads to the "smoothening" of the energetic distribution from the more distinct peaks on P-rich InP to the emission observed in Figure 2b,c, resulting in a quasi-continuous DOS. Additionally, as previously outlined, the relocation of the P-rich InP surface layer from the topmost atomic layer deeper within the material reduces the relative emission, decreasing the clarity of these surface peaks. The dense manifold of states in the TiO_2 conduction band increases the likelihood of transitions according to Marcus theory,[63,64] allowing for fast scattering of electrons between the layers. At 1.3 and 2.5 nm, direct emission from the P-rich p-InP layer is likely to still represent a significant fraction of emission, therefore thicker TiO_2 layers are required to conclusively ascertain the presence of scattering back-and-forth across the P-rich InP/TiO_2 interface.

Emission from states identified on the bare P-rich InP(100) surface, as well as after deposition of 1.3 and 2.5 nm TiO_2, is plotted as a function of time delay between pump and probe in UV – UV in **Figure 3a–c** respectively. Emission counts are normalized between the minimum and maximum recorded emission to enhance clarity in observing all temporal developments. Due to the previously described vacuum states, emission below C3 at 1.3 nm TiO_2 and below C2 at 2.5 nm TiO_2 is largely blocked, with only a small fraction of emission remaining. The surface state pinning the Fermi level on bare P-rich InP is destroyed after TiO_2 deposition, as determined earlier. Figure 3a illustrates the temporal evolution of emission from the bare P-rich InP surface, as initially

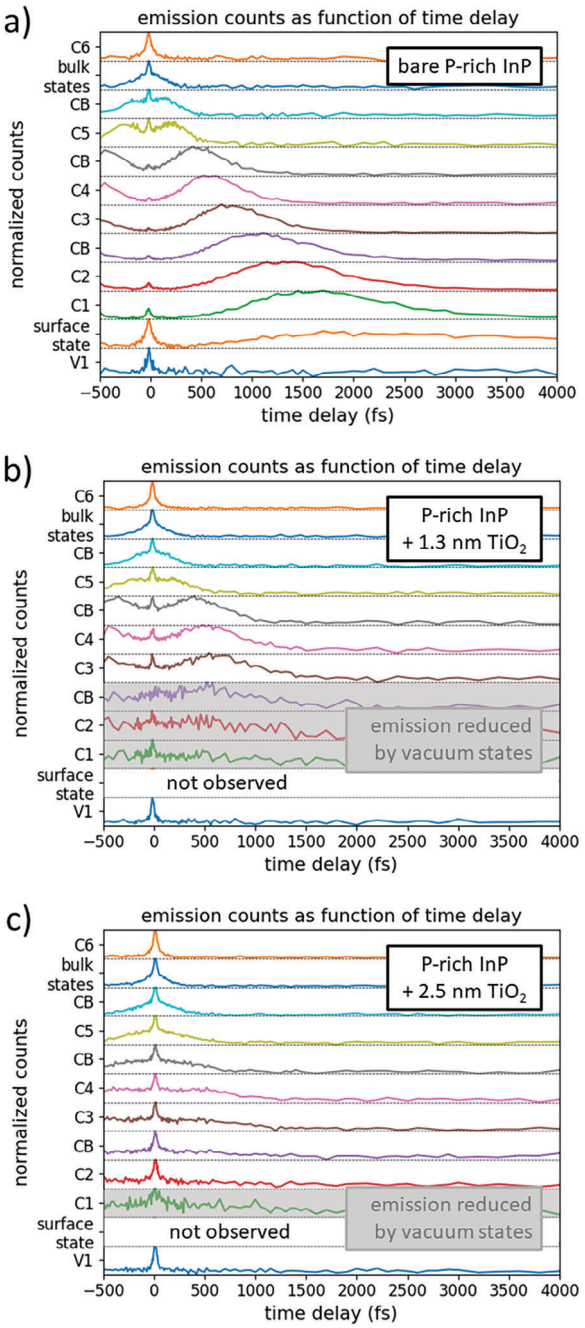

Figure 3. Temporal development of UV – UV emission from observed states from bare P-rich InP(100) in a), and after deposition of 1.3 and 2.5 nm TiO_2 in b,c). States which are blocked by vacuum states are denoted, the surface state pinning the Fermi level around the mid-gap on the bare P-rich InP surface is not observed after TiO_2 deposition.

explored in ref,[31] with a reconstructed electron thermalization path given in Figure S12 (Supporting Information).

From Table S2 (Supporting Information) we can determine that ≈34% of UV – UV emission at 1.3 nm and roughly 55% of emission at 2.5 nm TiO_2 occur within the TiO_2 layer, as emission counts are proportional to both pump-excitation densities and probe intensities, and therefore go with the square of absorption when using UV pump and probe. In comparison, VIS – UV yields up to 80% InP-layer emission at 1.3 nm TiO_2, and up to 66% at 2.5 nm. Notably, the TiO_2 layer itself does not exhibit clear states; instead, a central emission peak ≈0 fs delay appears across the observed states, indicating emission from the continuous TiO_2 DOS. This peak is sharper at 2.5 nm TiO_2 due to increased emission from the TiO_2 layer and is broadened relative to pump-probe cross-correlation by ≈10–20 fs across the delay range. This broadening likely stems from electron-electron scattering in the high DOS of TiO_2, coupled with high phonon availability leading to either ultrafast thermalization or scattering back to the InP layer.

In UV – UV emission, only a small decrease in lifetimes is observed for states above C4 (Figure 3). Peak occupation of C4 and C3 on the bare P-rich InP(100) surface occurs at 570 ± 50 and 760 ± 50 fs respectively. With 1.3 nm TiO_2, this shifts to 510 ± 50 and 610 ± 100 fs respectively, and with 2.5 nm TiO_2, it shifts to 480 ± 100 and ≈480 ± 100 fs, though less clearly discernible. Previous DFT analysis on the bare P-rich InP surface [31] suggested an increase in amplitude of C4 due to aligned states in the near-surface region. Additionally, Clady et al.[65] suggest that this energy corresponds to the CBM in the X-valley in bulk InP, with intervalley scattering from and to the Γ-valley occurring on the time-scale of tens to hundreds of fs. The timescale of processes in the InP bulk is expected to be minimally affected by TiO_2 deposition. However, surface resonance lifetimes are likely shortened by alternative thermalization paths the dense TiO_2 DOS adjacent to the interface, as well as potential defect sites induced during TiO_2 deposition. The modest 10% reduction in the lifetime of C4 after TiO_2 deposition, remaining consistent thereafter, suggests that the majority of state occupation involves electrons migrating from the InP bulk. Although some electrons thermalize at the surface, originating from the bulk-to-surface transition, their minor impact on C4 indicates that this process contributes only a fraction of electrons at this state. Furthermore, while the bulk-to-surface transition cluster of states acts as reservoir for scattering to other states, it seems inefficient in transporting hot electrons across the interface to adsorbate layers. C3 on the other hand appeared to be a surface-related feature in DFT analysis previously,[31] consistent with decreasing lifetimes observed with deposition until reaching C4 lifetimes, indicating no additional contribution to thermalizing electrons. At 2.5 nm TiO_2 (Figures 2c and 3c), states C2 and the CB state between C2 and C3 exhibit reduced time-dependent emission, with no apparent increase in lifetimes beyond C4. Due to the presence of vacuum states, lifetimes of C1 cannot be observed. This indicates that most photoexcited electrons in the InP bulk either reach the P-rich InP/TiO_2 interface around C1, or at C4 and energetically higher states. Thermalization below C4 occurs at the P-rich InP surface when TiO_2 is absent, whereas after deposition, it primarily occurs in the TiO_2 layer. This assignment of C3 and C2 to purely surface features is consistent with previous DFT results.[31] These findings hold significance in the realm of hot-carrier PV and PEC cells, indicating that hot electrons can reach the TiO_2 layer, and only thermalize within this adlayer (Figure S15, Supporting Information). Since P-rich InP surface states appear preserved under P-dimer oxidation during the deposition metal oxides like TiO_2, other adlayers could be explored for potentially reduced thermalization, thereby better preserving hot carrier lifetimes. InP surfaces grown via methods like MOVPE of-

fer an advantage here, compared to less defined surface preparation methods, as observing these sub-surface processes depends heavily on well-ordered interfaces to achieve observable signals. To allow for hot carriers to drive electrochemical reactions on the nano- to millisecond timescale, e.g quantum dots with suitable energetic alignment may be used. Specifically, aligning the QD CBM around InP C4 may allow for extraction and use of hot carriers from the InP bulk X-valley even through TiO_2 layers in the nm thickness range.

In a similar vein to lifetimes observed in UV – UV (Figure 3), lifetimes in VIS – UV were analyzed, with results detailed in the SI (Figures S14 and S15, Supporting Information). Again, peak occupancy of C3 and C4 shifts from 260 ± 40 and 470 ± 40 fs respectively on the bare P-rich InP surface, to 180 ± 40 and 220 ± 40 fs after depositing 1.3 nm TiO_2, and further to 180 ± 40 and 180 ± 40 fs after 2.5 nm TiO_2 deposition. This again highlights a decrease in C4 peak occupancy time after initial TiO_2 deposition, which then stabilizes at thicker layers. C3 lifetimes continue to decrease until they reach C4 lifetimes, indicating that most C3 electron occupation thermalizes through C4, making C4 the limiting factor in lifetime decreases. Notably, peak occupancy of C4 is achieved at lower delay times using the VIS compared to the UV pump, possibly due to the higher excitation intensity of the VIS pump and the additional thermalization duration added by the UV pump accessing the bulk-to-surface transition cluster of states. This trend is consistent at 2.5 nm TiO_2 (Figure S14c, Supporting Information), where states below C4 exhibit reduced time-dependent emission and no clear lengthening of lifetimes, corroborating previous analysis in UV – UV.

As reasoned above, at 1.3 and 2.5 nm TiO_2, around half or more emission occurs from the InP layer in UV – UV, while the majority of emission originates from the InP layer in VIS – UV. However, with a 10 nm TiO_2 layer applied In Figure 1j–l, only up to ≈4% of UV – UV emission, and 20% of VIS – UV emission occur from the InP layer. This is further limited by the mean free path length of electrons in TiO_2, reported by Bonn et al. as only 5Å,[66] while other sources suggest an electron escape depth of ≈3 nm.[53] Therefore, direct emission from the InP layer is not expected to significantly contribute to the observed tr-2PPE data, especially in UV – UV, with emission mainly occurring from the TiO_2 layer. Corresponding 3D-transient and time-development for VIS – UV are provided in Figure S16 (Supporting Information). XPS analysis reveals weak signals for In3d and P2p peaks (Figures S7 and S8, Supporting Information), albeit smaller in amplitude relative to the Ti2p peak. Given the time-resolved nature of tr-2PPE, and thereby shorter exposure times per delay slice and lower signal-to-noise ratio, this does not allow for observation of p-InP states in our experiments. In UV – UV with 10 nm TiO_2 (Figure 1l), a single clear emission peak is observed at a kinetic energy of 0.53 ± 0.05 eV, with the lower edge likely cutoff due to vacuum states. Emission amplitudes remain consistent regardless of time delay, indicating 1PPE from an occupied surface state. A leading edge at 0 fs delay toward higher kinetic energies is apparent, though states could not be reliably fitted in this energy range due to the low signal-to-noise ratio; time-dependent emission is provided in Figure S17a (Supporting Information). The energetic position of this surface state translates to −3.91 eV versus vacuum, corresponding to ≈0.2 eV below the InP CBM at 0.5 eV surface band bending,[31] and ≈0.7 eV below the InP CBM without band bending (Figure S12, Supporting Information). This state is then likely a bandgap surface state, with the large emission amplitude suggesting it is pinning the Fermi level.

In the VIS – UV spectrum with 10 nm TiO_2 (Figure 1k), the signal is symmetric around the zero-delay point, indicating minimal influence from the order of pump or probe beam arrival. Most of the signal decays within tens of femtoseconds, consistent with the pulse widths of VIS – and UV – beams. A time-independent signal ≈1 eV, just above the vacuum state cut-off, is observed, likely representing the upper-energy tail of UV 1PPE surface state emission. Peaks at delays in the tens of fs are visible within the ultrafast thermalization of electrons, seemingly corresponding to the previously described P-rich InP states. Literature 2PPE spectra of rutile TiO_2 surfaces measured by Onda et al.[52] and Argondizzo et al.[67,68] provide useful comparisons to our 10 nm TiO_2 VIS – UV spectra in Figure 1k. Their experiments utilized photon energies of 3.05, 3.44 and up to 3.95 eV, which are larger than the bandgap of rutile TiO_2 (3.03 eV).[57,58] Onda et al.[52] excited electrons from defect states in Ar+ sputtered rutile TiO_2 (110) and obtained a spectrum much like our 10 nm TiO_2 VIS – UV spectrum 63 (Figure 1k). Additionally, Onda et al. used Ar+ sputtering of the surface to enhance pumping from bulk defect states,[52] concluding that their emission spectra are mainly due to initial states in the bulk bandgap of TiO_2. The bandgap DOS of amorphous TiO_2 films depends sensitively on preparation conditions,[69] however the match to experiments and rough match to calculations in literature supports a similar cause for our emission in VIS – UV at 10 nm TiO_2 (Figure 1k).[70] More recently, Tanner et. al observed similar spectra on the anatase (101) TiO_2 surface, attributed to sub-surface bandgap polarons.[71] The similarity of these previously reported spectra to Figure 1k suggests that the overall shape of the VIS-UV time-dependent signal we observe for 10 nm TiO_2 is related to emission of electrons initially photoexcited from TiO_2 bandgap defect states. Both Onda et al. and Tanner et. al described photoemission pathways for their TiO_2 samples, where electrons are pumped from bulk bandgap defect states energetically below the Fermi level, into a continuous density of intermediate states in the TiO_2 conduction band.[52,71] This aligns well with our observed 2PPE kinetic energy spectrum of 10 nm TiO_2 VIS – UV measurements, matching experiments on TiO_2 alone.

In UV – UV (Figure 1k), emission is predominantly driven by 1PPE from the TiO_2 surface state, obscuring emission from bandgap DOS in TiO_2. Conversely, in VIS – UV, the higher photoexcitation density due to increased pump intensity leads to surface charges, causing an upward shift in the vacuum state-related cut-off energy. This indicates ongoing charge transfer from InP to the TiO_2 layer. While the bulk of UV photoelectron emission still originates in the TiO_2 layer, electrons photoexcited from TiO_2 bandgap defects may scatter across the TiO_2/P-rich InP interface, manifesting P-rich InP state positions in emission. If the p-InP surface states persist in the P-oxide interface layer and their wavefunctions extend into the TiO_2 layer (Figure S13, Supporting Information), this could result in polarons, facilitating ultrafast transfer between these states and the TiO_2 conduction band DOS. This phenomenon might explain the preservation of TiO_2 bulk bandgap defect DOS while reflecting the influence of interfacial states on electron relaxation. Xu et al. proposed a similar

electron injection mechanism from a III-V semiconductor into TiO_2, studying interfacial carrier separation at TiO2-coated GaP using fs transient reflectance spectroscopy[47,72] for TiO_2 layer thicknesses up to 35 nm. They reported a time constant of 32 fs for charge separation at the direct interface, consistent with the carrier dynamics observed in our 2PPE measurements. Similarly, Yang et al. used time-resolved photoinduced reflectance to monitor the carrier dynamics at the p-$GaInP_2$/TiO_2 interface for TiO_2 thicknesses between 0.5 and 35 nm.[73]

The upper edge of the time-dependent signal in VIS – UV (Figure 1k) is ≈2.81 ± 0.10 eV, likely corresponding to the upper edge of bandgap defect states and hence the Fermi level at the 10 nm TiO_2 surface. The emission signals decay within tens of fs of delay time between VIS pump and UV probe, suggesting a correlation to 2PPE emission using one VIS and one UV photon. This aligns the Fermi level at −3.96 ± 0.10 eV versus vacuum, in close agreement with the value obtained for the 1PPE peak observed in UV – UV at −3.91 ± 0.05 eV. Therefore, this state appears to indeed be a TiO_2 surface state pinning the Fermi level.

The emission cut-off related to surface charging limits the observation of all conduction band states in the deposited TiO_2 layers. The lowest observed cut-off energies at 1.3 and 2.5 nm TiO_2 are 0.73 and 0.66 eV, respectively, in the corresponding UV – UV measurements (Figure 1f,i). Above these cut-offs, emission from likely conduction band states was detected, setting an upper limit for the TiO_2 CBM versus vacuum. This suggests an alignment at 1.3 nm of the TiO_2 CBM positioned energetically at most 0.06 ± 0.10 eV above the InP CBM, and with theTiO_2 CBM at least 0.06 ± 0.10 eV below the InP CBM at 2.5 nm TiO_2. The uncertainties are aggregated from uncertainties in state positions before and after TiO_2 deposition. In the 10 nm TiO_2 layer (Figure 1k), a lower bound for the TiO_2 CBM is determined by the position of the TiO_2 surface state pinning the Fermi level, indicating that the TiO_2 CBM is less than 0.25 ± 0.10 eV below the InP CBM. Fitting indicated the presence of the P-rich InP C1 state below the cut-off energies at each TiO_2 thickness in Figure 1, although accurate fitting was challenging. Therefore, the TiO_2 and p-InP conduction bands seem to align remarkably well, consistent with literature on this interface.[3–5,8,62]

2.1.1. Annealing the 10 nm Tio_2 Surface

The previously discussed 10 nm TiO_2 layer deposited on the P-rich InP surface was subjected to annealing using the ALD apparatus to investigate alterations in electron thermalization. Annealing was conducted at 300 °C, a temperature below the decomposition threshold of the P-rich InP surface at ≈356 ± 5 K,[74] for 3 h in the presence of hydrogen. Hydrogen is commonly used as carrier gas in MOVPE-preparation and different gas environments are known to change the surface reconstruction of the P-rich InP(100) essentially, due to its H-stabilized nature [see below]. Hence, hydrogen was used for the preparation and annealing procedure of the surface to avoid desorption of hydrogen involved in the P-rich InP/TiO_2 interface affecting observed states.[75] Annealing TiO_2 at sample temperatures above 350 °C typically results in crystalline structures, while lower temperatures lead to amorphous formations.[76,77] As amorphous

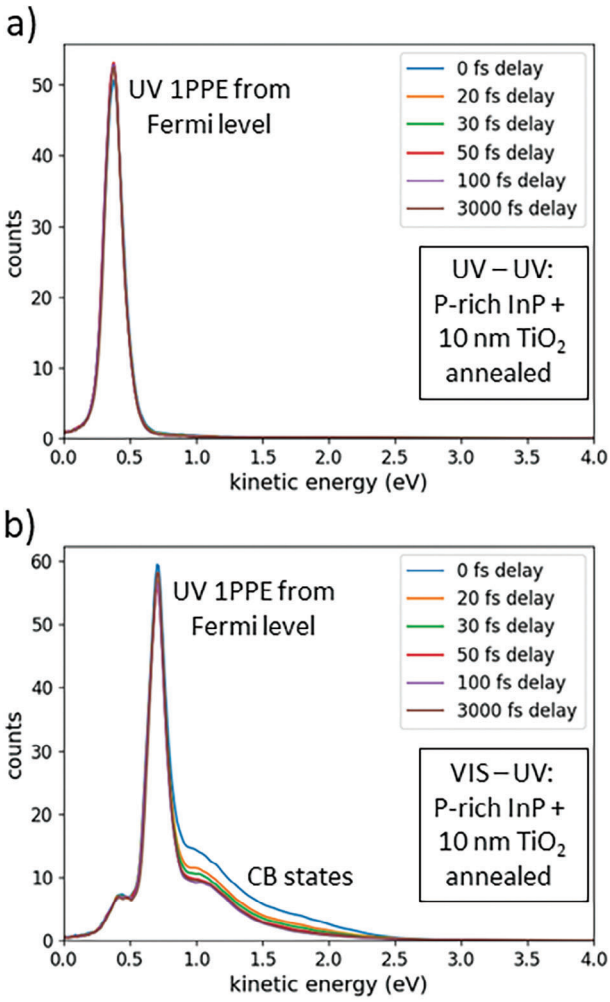

Figure 4. tr-2PPE spectra of the 10 nm TiO_2 on P-rich InP surface after annealing are given in a,b), in UV-UV and VIS-UV respectively. 1PPE from around the Fermi level is the prominent feature in both excitation schemes, CB states appear to be observed in VIS – UV (b).

TiO_2 layers have been linked to the highest PEC efficiencies in literature,[3,5] the annealing temperature was deliberately kept below crystallization thresholds to prevent the formation of a well-ordered lattice and to preserve the integrity of the InP layer, with LEED imaging indicating no crystallinity associated with rutile or anatase TiO_2. Subsequent to annealing, significant alterations in tr-2PPE were observed. In UV – UV (**Figure 4a**), a single emission peak emerges at 0.38 eV kinetic energy, accompanied by an emission tail at higher energies, albeit lacking clear peaks in the time-dependent emission (Figure S17b, Supporting Information). This likely corresponds to emission from the rising occupied DOS around the Fermi level as well as potential surface states around the Fermi level. Given the lack of clear evidence for surface states around the Fermi level from UPS (Figure S9, Supporting Information) as well as from the TiO_2 bandgap states, it cannot be clearly discerned which contribution to emission is larger. Murakami et al. reported that annealing a TiO_2 layer following exposure to $TiCl_4$ lowered the conduction band edge position by 110 mV, resulting in enhanced photovoltaic perfor-

mance in their perovskite absorber based system.[78] This correlates well to the reduced energetic position of the Fermi level after annealing, as $TiCl_4$ was used as the Ti precursor. Moreover, Liu et al. highlighted that TiO_2 surfaces treated with TiCl4 exposure and subsequent sintering exhibited an increased ratio of Ti^{3+} to Ti^{4+},[79] with Ti^{3+} acting as the donor species in the TiO_2 film. This shift toward Ti^{3+} resulted in a movement of the Fermi level toward the conduction band, leading to an increased VOC in their perovskite absorber-based cells due to improved band alignment facilitating electron extraction. In a related study, Mansfeldova et al.[80] reported a range for the CBM of crystalline TiO_2 surfaces between 3.60 and 4.63 eV below vacuum energy, depending on surface reconstruction, with Fermi levels only marginally below the CBM due to the highly n-doped nature of their samples. This information supports the interpretation that the emission observed at 0.34 eV in UV-UV after annealing the 10 nm TiO_2 layer (Figure 4a) likely is located at the Fermi level, estimated to be at –4.15 eV versus vacuum. Additionally, Onda et al. associated the upper end of the defect DOS, located ≈2.7 ± 0.1 eV kinetic energy in our measurement, with the Fermi level position, as it represents the upper edge of the bandgap defect DOS. Given the emission pattern observed via a combination of VIS and UV photon, the estimated Fermi level position of –4.12 eV correlates well with the surface state/Fermi level position observed in UV – UV.

In the VIS – UV spectrum (Figure 4b), this peak appears to be partially cropped off at 0.30 eV, likely due to surface charging and the work function edge. This effect arises because the photon energy of the VIS beam is lower than that of the UV beams, preventing direct 1PPE from the observed surface state. The decrease in surface charging observed in VIS – UV after annealing compared to before is likely due to a reduction in surface defects following the annealing process, as reported in literature.[52] The presence of a time-independent peak at 0.71 eV kinetic energy likely corresponds also to emission from around the Fermi level but is associated with direct 2PPE emission induced by the VIS pump. Given that two VIS photons collectively provide ≈4.66 eV, compared to 4.44 eV of one UV photon in this measurement, the increased kinetic energy in VIS 2PPE relative to UV 1PPE results in the observed double feature. Although time-dependent emission is evident in Figure 4b at kinetic energies above these peaks, identifying states in this region is challenging due to the dominance of the relatively large 1PPE peak. Another sample after deposition of 14 nm TiO_2 was found to show similar features to the 10 nm TiO_2 sample after annealing, a detailed description of the measurement is found in Figure S18 and Note S3 (Supporting Information).

The discrete interface states observed after deposition of TiO_2 layers up to 10 nm (Figure 1) are suggested as a reference system for the study of electron transfer from adsorbates and surface layers, e.g. nanodot plasmonics and QD. As the states at the P-rich InP/TiO_2 interface are discrete, observing changes in emission amplitude may give information about the energy distribution and timing of electrons reaching the interface. To reduce the effects of thermalization within the TiO_2 layer, using layers below 2.5 nm thickness may be preferable. The chemically well-studied nature of the TiO_2 surface will be of advantage here, as many systems can be easily deposited or synthesized in situ.

Comparison of the time-dependent components of the VIS – UV spectrum (**Figure** 5b) after annealing the 10 nm TiO_2 layer

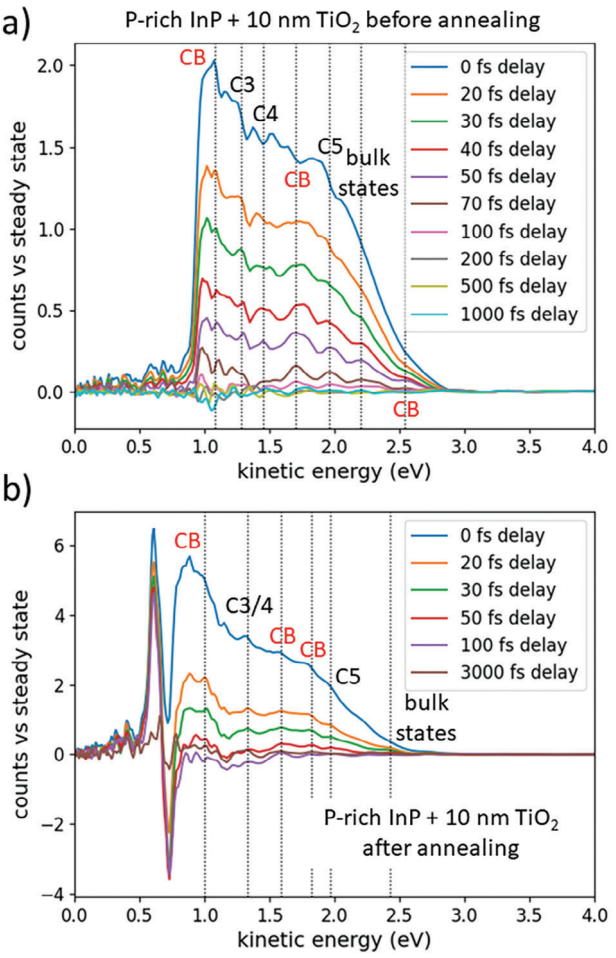

Figure 5. Differences in emission in VIS-UV between different time delays to measurement at 5000 fs, where emission had stabilized. The 10 nm TiO_2 on P-rich InP is shown in a), and after annealing in b). The dotted vertical lines denote kinetic energies at which emission peaks are observed during thermalization of hot carriers toward the CBM, states become less distinctive after annealing.

with those before annealing (Figure 5a) reveals a visually similar emission shape, with the width and energetic position of the features falling within the uncertainty of the surface before annealing.

Figure 5 displays the temporal evolution of state occupation in VIS – UV emission at the 10 nm TiO_2 layer before and after annealing, depicted in (a) and (b) respectively. Following annealing, significant surface state emission is evident in Figure 5b ≈0.6 eV, though this does not correspond to an electronic state. Peaks are discernible both before and after annealing, with C2 and below cut-off due to vacuum states as well as the surface state emission signal. Before annealing, peaks are clearly visible at delays in the tens of fs, encompassing all previously described P-rich InP states. However, after annealing, these peaks become notably less distinct, suggesting that the heat treatment has compromised or eradicated these P-rich InP states. While the sample temperature of 300 °C during annealing should not lead to decomposition of the P-rich InP surface itself, it may provide the activation energy for a restructuring of the P-rich InP/TiO_2 interface, or relaxation

of lattice-matching at this interface. This could potentially result in a less ordered interface than before, thereby disrupting the distinct surface states observed prior to annealing. Notably, even annealing at 300 °C seems to compromise or obliterate the surface states on InP. Consequently, when creating rutile or anatase TiO_2 surfaces through annealing above 350 °C, InP surface states would always be destroyed. This observation may elucidate the higher- than-expected performance of amorphous TiO_2 on InP-based absorbers,[3,40] particularly in PEC applications, which may be less contingent on TiO_2 crystallinity and more influenced by preserving a well-ordered interface between absorber and protective layer. Modifying the interface could introduce additional defect sites that hinder transmission, while also removing energetically distinct states and facilitating efficient charge transfer across the InP / TiO_2 interface.

3. Conclusion

We investigated the electron excitation dynamics and -pathways on phosphorus-terminated, p(2 × 2)/c(4 × 2)-reconstructed InP(100) surfaces following the deposition of TiO_2 layers with varying thicknesses via ALD. Conduction band surface resonances previously identified on the P-rich p-InP surface remained intact post-TiO_2 deposition, maintaining their energetic positions within the range of ≈−3.7 and −1.7 eV relative to vacuum energy. Photoexcited electrons follow a trajectory through the InP bulk-to surface transition cluster of states and InP C4, traversing P-rich InP surface states until reaching the TiO_2 layer. Within this layer, an alternative thermalization path to the InP layer is offered, reducing lifetimes of states energetically below InP C4. Notably, even at 10 nm TiO_2 layer thickness, the thermalization behavior is impacted by electron scattering between the dense TiO_2 CB DOS and the discrete P-rich InP surface/interfacial states. These discrete states carry profound implications for the design of photovoltaic or electrochemical devices incorporating P-rich InP protected by TiO_2. Annealing the samples at 300 °C induces a notable shift in the TiO_2 CBM, transitioning toward a more classically continuous DOS, a change likely attributed to reconstruction of the interface to be less well-structured. The discrete states situated above the CBM offer opportunities for applications such as hot carrier cells, facilitating electron extraction to the TiO_2 layer without prior thermalization to the InP CBM. This is particularly significant, considering previous findings on phonon bottlenecking effects in bulk InP,[81] a critical aspect for the design of such cells. Crafting interfaces that leverage these discrete states will likely necessitate low-temperature processing and the use of thin TiO_2 layers in the nanometer range, as surface relaxation may compromise the observed state discreteness.[81]

4. Experimental Section

Sample Preparation in MOVPE: InP(100) samples with a P-rich, p(2 × 2)/c(4 × 2) surface reconstruction (Figure S1, Supporting information) were prepared in a horizontal-flow MOCVD reactor (Aixtron, AIX-200) on p-doped InP(100) substrates with a doping concentration of 2×10^{18} cm^{-3} (Zn-doped) and a 0.1° miscut toward the [111] direction. The sample preparation was described in detail in a previous paper.[31]

Sample Characterization Using XPS: XPS measurements utilized a SPECS Focus 500 monochromator and Phoibos 100 electron analyzer, using Al Kα radiation at 1486.74 eV. The XP spectra were measured at a 90° photoelectron take-off angle, and the angle between the X-ray source and the analyzer was 54.7°. The high-resolution core level peaks were measured with a pass energy of 10 eV, in energy steps of 0.05 eV.

Surface Modification Using ALD: Surface modification of the P-rich InP(100) surface was performed using ALD, a gas phase deposition technique with which ultrathin films were grown in sub-monolayer steps through alternating half-cycles, depositing oxygen and a metal respectively in the case of metal oxide deposition. The reactions of gas phase precursors with the surface during the ALD half-cycles were self-limiting,[82] enabling growth control at the single atom layer level. The self-limiting half-cycles enable uniform and conformal deposition over large areas and diverse substrates. In this study, titanium dioxide thin films were deposited on the P-rich InP(100) samples utilizing a custom-built, hot-wall stainless steel ALD reactor. This reactor operates in an in-line configuration with an ultrahigh vacuum (UHV) chamber, facilitating XPS measurements for elemental composition and chemical state analysis during film growth. The reactor was continuously pumped by a turbomolecular pump backed-up by a roughing pump, reaching a base pressure of $2–4 \times 10^{-7}$ mbar. Titanium tetrachloride ($TiCl_4$, 99.999% Sigma-Aldrich) and H_2O were used as the titanium and oxygen precursors, respectively; both precursors were maintained at room temperature during deposition. The precursors were alternatingly introduced into the system via ALD diaphragm valves using the vapor draw method (i.e., without using a carrier gas). While the reactor wall was heated to 125 °C, the tubing and fittings were unheated. The substrate temperature remained constant at 200 °C for all depositions. After each precursor exposure, a pump/purge/pump step was carried out, involving 15 s of pumping, followed by a 100 ms Ar purge, and concluding with another 15 s of pumping. This ensured that the base pressure could be consistently maintained at $3–5 \times 10^{-6}$ mbar. To conclude each deposition cycle, an additional H_2O pulse/purge sequence was carried out. During experiments investigating the effects of the ALD process itself, the $TiCl_4$ pulse and purge steps were omitted, keeping the rest of the process unchanged. This ALD deposition cycle is described in Table S1 (Supporting Information). An example of a deposited TiO_2 layer is shown in Figure S2 (Supporting Information), with AFM showing a wave-shaped surface coverage.

Time-Resolved Two-Photon Photoemission Spectroscopy: In tr-2PPE, an ultrashort laser pulse photoexcites ("pumps") electrons to energy levels below the vacuum energy, from where they thermalize into unoccupied states (Figures S3 and S5, Supporting Information). After a variable time, delay a lower-intensity probe pulse photoemits the electrons into the vacuum, and their energy distribution as a function of pump-probe delay was recorded. This allows for determination of state energies and -lifetimes, the latter by scanning over varying time delays in steps as small as 5 fs. Near-surface ultrafast electron dynamics through both occupied and unoccupied states were observed, particularly unoccupied conduction band states, which could not be accessed by single-photon emission methods such as XPS/UPS.[83,84] In previous studies in this group the information depth of n-type InP was estimated at 45 Å,[30] which means that both bulk and surface features as well as bulk-to-surface transitions could be captured.

Pump and probe photon energies could be varied to allow for pumped electrons to access different energy levels. As a result, a difference between pump and probe energy creates an asymmetry in the time-domain about the zero-delay point. The experimental procedure for the tr-2PPE measurement was described.[31] Visible light pump pulses were usually set ≈533 nm (2.33 eV) and 3.3 nJ pulse energy with a FWHM of 40 fs at the sample. Ultraviolet (UV) pump and probe pulses were tuned to ≈276 nm (4.49 eV) at 30 fs FWHM. The UV pump was usually set to 0.26 nJ pulse energy, the UV probe to ≈0.13 nJ. To detect photoemitted electrons a time-of-flight (TOF) detector with a 7.3° acceptance angle was positioned 3–5 mm from the sample surface. The detector has an energy resolution of ca. 50 meV, with the spectral width of photon energies of similar magnitude. The angle between the pump and probe beams to the sample was 45°. Pump and probe intensities were adjusted to prevent charging of the

surface and to avoid influencing the observed electron dynamics at higher emission rates. The spot size of the pump-probe overlap was of the order of 100 µm, resulting in pump fluences below 100 nJ cm^{-2} for the VIS pump, and below 10 nJ cm^{-2} for UV excitation. In the resulting tr-2PPE plots, peaks were fitted using a custom-written composite-Voigt script, including binning and gaussian smoothing. The procedure was described in more detail.[31] All tr-2PPE measurements were repeated several times to avoid artifacts or features related to local defects, with the most representative measurements given.

Density-Functional Theory Calculations: Density-functional theory (DFT) calculations were performed using the Vienna Ab-Initio Simulation Package (VASP).[85] The electron exchange and correlation effects were treated within the generalized gradient approximation (GGA) using the PBE functional.[86] The electron–ion interaction was described by the projector-augmented wave (PAW) scheme.[87,88] The surfaces were modeled using periodic supercells, consisting of a slab of twelve atomic layers. A vacuum region of ≈15 Å was used to decouple the material slab from its periodic image. The electric field in the vacuum region resulting from the two nonequivalent slab surfaces was quenched using a dipole correction. The wave functions were expanded into plane waves up to an energy cutoff of 500 eV. The surface Brillouin zone was sampled using a Γ-centered 4 × 4 k-point mesh. The uppermost six atomic layers were structurally relaxed until the forces acting on the atoms were below 0.02 eV $Å^{-1}$, while the remaining six bottom layers were kept frozen in the bulk position. To determine the most favorable adsorption sites for single water molecules and hydroxyl groups, the surface unit cell was sampled using a mesh of 64 equidistant points.

Supporting Information

Supporting Information is available from the Wiley Online Library or from the author.

Acknowledegements

The authors are grateful to acknowledge the financial support of German Research Foundation (DFG project PAK 981, project no. FR 4025/2-1, KR4816/1-1, HA3096/14-1, and SCHM1361/26). The authors thank the Paderborn Center for Parallel Computing and the Höchstleistungs-Rechenzentrum Stuttgart (HLRS) for grants of high-performance computer time. The authors also express gratitude for financial support provided by the German Federal Ministry of Education and Research (H2Demo project no. 03SF0619).

Open access funding enabled and organized by Projekt DEAL.

Conflict of Interest

The authors declare no conflict of interest.

Author Contributions

All authors have given approval to the final version of the manuscript.

Data Availability Statement

The data that support the findings of this study are available from the corresponding author upon reasonable request.

Keywords

carrier dynamics, electronic structure, energy, indium phosphide, semiconductors, surface science, titanium dioxide

Received: May 31, 2024
Revised: August 15, 2024
Published online: October 16, 2024

[1] R. van de Krol, B. A. Parkinson, *MRS Energy Sustainability* **2017**, *4*, E13.
[2] W.-H. Cheng, M. H. Richter, M. M. May, J. Ohlmann, D. Lackner, F. Dimroth, T. Hannappel, H. A. Atwater, H.-J. Lewerenz, *ACS Energy Lett.* **2018**, *3*, 1795.
[3] X. Yin, C. Battaglia, Y. Lin, K. Chen, M. Hettick, M. Zheng, C.-Y. Chen, D. Kiriya, A. Javey, *ACS Photonics* **2014**, *1*, 1245.
[4] A. G. Muñoz, C. Heine, H. W. Klemm, T. Hannappel, N. Szabo, H.-J. Lewerenz, *ECS Trans.* **2011**, *35*, 141.
[5] Y. Lin, R. Kapadia, J. Yang, M. Zheng, K. Chen, M. Hettick, X. Yin, C. Battaglia, I. D. Sharp, J. W. Ager, A. Javey, *J. Phys. Chem. C* **2015**, *119*, 2308.
[6] E. Aharon-Shalom, A. Heller, *J. Electrochem. Soc.* **1982**, *129*, 2865.
[7] M. H. Lee, K. Takei, J. Zhang, R. Kapadia, M. Zheng, Y.-Z. Chen, J. Nah, T. S. Matthews, Y.-L. Chueh, J. W. Ager, A. Javey, *Angew. Chem., Int. Ed.* **2012**, *51*, 10760.
[8] L. Gao, Y. Cui, R. H. J. Vervuurt, D. van Dam, R. P. J. van Veldhoven, J. P. Hofmann, A. A. Bol, J. E. M. Haverkort, P. H. L. Notten, E. P. A. M. Bakkers, E. J. M. Hensen, *Adv. Funct. Mater.* **2016**, *26*, 633.
[9] P. Vogt, A. M. Frisch, T.h. Hannappel, S. Visbeck, F. Willig, C. Jung, R. Follath, W. Braun, W. Richter, N. Esser, *Appl. Surf. Sci.* **2000**, *166*, 190.
[10] J. Wang, F. Sciarrino, A. Laing, M. G. Thompson, *Nat. Photonics* **2020**, *14*, 273.
[11] M. Smit, K. Williams, J. van der Tol, *APL Photonics* **2019**, *4*, 050901.
[12] Y. Wang, Y. Jiao, K. Williams, *APL Photonics* **2024**, *9*, 050902.
[13] D. E. Aspnes, A. A. Studna, *Phys. Rev. B* **1983**, *27*, 985.
[14] M. Nandy, A. Paszuk, M. Feifel, C. Koppka, P. Kleinschmidt, F. Dimroth, T. Hannappel, *Cryst. Growth Des.* **2021**, *21*, 5603.
[15] O. Supplie, O. Romanyuk, C. Koppka, M. Steidl, A. Nägelein, A. Paszuk, L. Winterfeld, A. Dobrich, P. Kleinschmidt, E. Runge, T. Hannappel, *Prog. Cryst. Growth Charact. Mater.* **2018**, *64*, 103.
[16] J. van Engelen, S. Reniers, J. Bolk, K. Williams, J. van der Tol, Y. Jiao, presented at 2019 Compd. Semicond. Week CSW, Nara, Japan, May **2019**.
[17] Y. Hu, D. Liang, K. Mukherjee, Y. Li, C. Zhang, G. Kurczveil, X. Huang, R. G. Beausoleil, *Light: Sci. Appl.* **2019**, *8*, 93.
[18] Z. Yan, Y. Han, L. Lin, Y. Xue, C. Ma, W. K. Ng, K. S. Wong, K. M. Lau, *Light: Sci. Appl.* **2021**, *10*, 200.
[19] C. Latz, T. Asshauer, C. Rathjen, A. Mirshahi, *Micromachines* **2021**, *12*, 122.
[20] P. H. Hahn, W. G. Schmidt, *Surf. Rev. Lett.* **2003**, *10*, 163.
[21] L. Li, B.-K. Han, Q. Fu, R. F. Hicks, *Phys. Rev. Lett.* **1999**, *82*, 1879.
[22] D. C. Moritz, I. A. Ruiz Alvarado, M. A. Zare Pour, A. Paszuk, T. Frieß, E. Runge, J. P. Hofmann, T. Hannappel, W. G. Schmidt, W. Jaegermann, *ACS Appl. Mater. Interfaces* **2022**, *14*, 47255.
[23] M. M. May, H.-J. Lewerenz, T. Hannappel, *J. Phys. Chem. C* **2014**, *118*, 19032.
[24] W. G. Schmidt, P. H. Hahn, F. Bechstedt, N. Esser, P. Vogt, A. Wange, W. Richter, *Phys. Rev. Lett.* **2003**, *90*, 126101.
[25] R. Sciotto, I. A. Ruiz Alvarado, W. G. Schmidt, *Surfaces* **2024**, *7*, 79.
[26] W. G. Schmidt, J. Bernholc, F. Bechstedt, *Appl. Surf. Sci.* **2000**, *166*, 179.
[27] W. G. Schmidt, F. Bechstedt, N. Esser, M. Pristovsek, C. Schultz, W. Richter, *Phys. Rev. B* **1998**, *57*, 14596.
[28] L. Töben, L. Gundlach, R. Ernstorfer, R. Eichberger, T. Hannappel, F. Willig, A. Zeiser, J. Förstner, A. Knorr, P. H. Hahn, W. G. Schmidt, *Phys. Rev. Lett.* **2005**, *94*, 067601.
[29] L. Töben, L. Gundlach, T. Hannappel, R. Ernstorfer, R. Eichberger, F. Willig, *Appl. Phys. A* **2004**, *78*, 239.
[30] L. Töben, T. Hannappel, R. Eichberger, K. Möller, L. Gundlach, R. Ernstorfer, F. Willig, *J. Cryst. Growth* **2003**, *248*, 206.
[31] J. Diederich, J. Velasquez Rojas, M. A. Zare Pour, I. A. Ruiz Alvarado, A. Paszuk, R. Sciotto, C. Höhn, K. Schwarzburg, D. Ostheimer, R.

Eichberger, W. G. Schmidt, T. Hannappel, R. van de Krol, D. Friedrich, *J. Am. Chem. Soc.* **2024**, *146*, 8949.
[32] J. L. Young, M. A. Steiner, H. Döscher, R. M. France, J. A. Turner, T. G. Deutsch, *Nat. Energy* **2017**, *2*, 17028.
[33] S. Hu, N. S. Lewis, J. W. Ager, J. Yang, J. R. McKone, N. C. Strandwitz, *J. Phys. Chem. C* **2015**, *119*, 24201.
[34] S. Hu, M. R. Shaner, J. A. Beardslee, M. Lichterman, B. S. Brunschwig, N. S. Lewis, *Science* **2014**, *344*, 1005.
[35] D. Bae, S. Shayestehaminzadeh, E. B. Thorsteinsson, T. Pedersen, O. Hansen, B. Seger, P. C. K. Vesborg, S. Ólafsson, I. Chorkendorff, *Sol. Energy Mater. Sol. Cells* **2016**, *144*, 758.
[36] B. Seger, T. Pedersen, A. B. Laursen, P. C. K. Vesborg, O. Hansen, I. Chorkendorff, *J. Am. Chem. Soc.* **2013**, *135*, 1057.
[37] B. Mei, T. Pedersen, P. Malacrida, D. Bae, R. Frydendal, O. Hansen, P. C. K. Vesborg, B. Seger, I. Chorkendorff, *J. Phys. Chem. C* **2015**, *119*, 15019.
[38] B. Abendroth, T. Moebus, S. Rentrop, R. Strohmeyer, M. Vinnichenko, T. Weling, H. Stöcker, D. C. Meyer, *Thin Solid Films* **2013**, *545*, 176.
[39] A. J. Kaufman, R. A. Krivina, M. Shen, S. W. Boettcher, *ACS Energy Lett.* **2022**, *7*, 541.
[40] J. Gu, Y. Yan, J. L. Young, K. X. Steirer, N. R. Neale, J. A. Turner, *Nat. Mater.* **2015**, *15*, 456.
[41] T. Moehl, J. Suh, L. Sévery, R. Wick-Joliat, S. D. Tilley, *ACS Appl. Mater. Interfaces* **2017**, *9*, 43614.
[42] S. Hu, M. H. Richter, M. F. Lichterman, J. A. Beardslee, T. Mayer, B. S. Brunschwig, N. S. Lewis, *J. Phys. Chem. C* **2016**, *120*, 3117.
[43] A. G. Scheuermann, J. P. Lawrence, K. W. Kemp, T. Ito, A. Walsh, C. E. D. Chidsey, P. K. Hurley, P. C. McIntyre, *Nat. Mater.* **2015**, *15*, 99.
[44] M. T. McDowell, M. F. Lichterman, A. I. Carim, R. Liu, S. Hu, B. S. Brunschwig, N. S. Lewis, *ACS Appl. Mater. Interfaces* **2015**, *7*, 15189.
[45] R. W. Johnson, A. Hultqvist, S. F. Bent, *Mater. Today* **2014**, *17*, 236.
[46] M. P. Seah, W. A. Dench, *Surf. Interface Anal.* **1979**, *1*, 2.
[47] Z. Xu, B. Hou, F. Zhao, Z. Cai, H. Shi, Y. Liu, C. L. Hill, D. G. Musaev, M. Mecklenburg, S. B. Cronin, T. Lian, *Nano Lett.* **2021**, *21*, 8017.
[48] J. Qiu, G. Zeng, P. Pavaskar, Z. Li, S. B. Cronin, *Phys. Chem. Chem. Phys.* **2014**, *16*, 3115.
[49] G. Zeng, J. Qiu, P. Pavaskar, Z. Li, S. B. Cronin, *ACS Catal.* **2014**, *4*, 3512.
[50] G. Chen, S. B. Visbeck, D. C. Law, R. F. Hicks, *J. Appl. Phys.* **2002**, *91*, 9362.
[51] H. Ali-Löytty, M. Hannula, J. Saari, L. Palmolahti, B. D. Bhuskute, R. Ulkuniemi, T. Nyyssönen, K. Lahtonen, M. Valden, *ACS Appl. Mater. Interfaces* **2019**, *11*, 2758.
[52] K. Onda, B. Li, H. Petek, *Phys. Rev. B* **2004**, *70*, 045415.
[53] G. A. Somorjai, B. E. Bent, *Phys. Today* **1995**, *48*, 58.
[54] H. Petek, S. Ogawa, *Prog. Surf. Sci.* **1997**, *56*, 239.
[55] M. Atif, W. A. Farooq, A. Fatehmulla, M. Aslam, S. M. Ali, *Materials* **2015**, *8*, 355.
[56] H. Tang, F. Lévy, H. Berger, P. E. Schmid, *Phys. Rev. B* **1995**, *52*, 7771.
[57] D. O. Scanlon, C. W. Dunnill, J. Buckeridge, S. A. Shevlin, A. J. Logsdail, S. M. Woodley, C. R. A. Catlow, M. J. Powell, R. G. Palgrave, I. P. Parkin, G. W. Watson, T. W. Keal, P. Sherwood, A. Walsh, A. A. Sokol, *Nat. Mater.* **2013**, *12*, 798.
[58] T. Luttrell, S. Halpegamage, J. Tao, A. Kramer, E. Sutter, M. Batzill, *Sci. Rep.* **2014**, *4*, 4043.
[59] H. Tang, H. Berger, P. E. Schmid, F. Lévy, G. Burri, *Solid State Commun.* **1993**, *87*, 847.
[60] A. Amtout, R. Leonelli, *Phys. Rev. B* **1995**, *51*, 6842.
[61] C. A. Gueymard, *Sol. Energy* **2004**, *76*, 423.
[62] L. A. Cipriano, G. Di Liberto, S. Tosoni, G. Pacchioni, *J. Phys. Chem. C* **2021**, *125*, 11620.
[63] N. B. Taylor, I. Kassal, *Chem. Sci.* **2018**, *9*, 2942.
[64] R. A. Marcus, N. Sutin, *Biochim. Biophys. Acta* **1985**, *811*, 265.
[65] R. Clady, M. J. Y. Tayebjee, P. Aliberti, D. König, N. J. Ekins-Daukes, G. J. Conibeer, T. W. Schmidt, M. A. Green, *Prog. Photovolt. Res. Appl.* **2012**, *20*, 82.
[66] M. Bonn, F. Wang, J. Shan, T. F. Heinz, E. Hendry, in *Femtochemistry Femtobiology* (Eds.: M. M. Martin, J. T. Hynes), Elsevier, Amsterdam **2004**, p. 517.
[67] A. Argondizzo, S. Tan, H. Petek, *J. Phys. Chem. C* **2016**, *120*, 12959.
[68] A. Argondizzo, X. Cui, C. Wang, H. Sun, H. Shang, J. Zhao, H. Petek, *Phys. Rev. B* **2015**, *91*, 155429.
[69] A. Soussi, A. Ait Hssi, M. Boujnah, L. Boulkadat, K. Abouabassi, A. Asbayou, A. Elfanaoui, R. Markazi, A. Ihlal, K. Bouabid, *J. Electron. Mater.* **2021**, *50*, 4497.
[70] M. Landmann, T. Köhler, S. Köppen, E. Rauls, T. Frauenheim, W. G. Schmidt, *Phys. Rev. B* **2012**, *86*, 064201.
[71] A. J. Tanner, B. Wen, Y. Zhang, L.-M. Liu, H. H. Fielding, A. Selloni, G. Thornton, *Phys. Rev. B* **2021**, *103*, L121402.
[72] Z. Xu, B. Hou, F. Zhao, S. Suo, Y. Liu, H. Shi, Z. Cai, C. L. Hill, D. G. Musaev, M. Mecklenburg, S. B. Cronin, T. Lian, *J. Am. Chem. Soc.* **2023**, *145*, 2860.
[73] Y. Yang, J. Gu, J. L. Young, E. M. Miller, J. A. Turner, N. R. Neale, M. C. Beard, *Science* **2015**, *350*, 1061.
[74] R. F. C. Farrow, *J. Phys. Appl. Phys.* **1974**, *7*, 2436.
[75] H. Döscher, K. Möller, T. Hannappel, *J. Cryst. Growth* **2011**, *318*, 372.
[76] C. Jin, B. Liu, Z. Lei, J. Sun, *Nanoscale Res. Lett.* **2015**, *10*, 95.
[77] D. Saha, R. S. Ajimsha, K. Rajiv, C. Mukherjee, M. Gupta, P. Misra, L. M. Kukreja, *Appl. Surf. Sci.* **2014**, *315*, 116.
[78] T. N. Murakami, T. Miyadera, T. Funaki, L. Cojocaru, S. Kazaoui, M. Chikamatsu, H. Segawa, *ACS Appl. Mater. Interfaces* **2017**, *9*, 36708.
[79] Z. Liu, Q. Chen, Z. Hong, H. Zhou, X. Xu, N. De Marco, P. Sun, Z. Zhao, Y.-B. Cheng, Y. Yang, *ACS Appl. Mater. Interfaces* **2016**, *8*, 11076.
[80] V. Mansfeldova, M. Zlamalova, H. Tarabkova, P. Janda, M. Vorokhta, L. Piliai, L. Kavan, *J. Phys. Chem. C* **2021**, *125*, 1902.
[81] Y. Zhang, G. Conibeer, S. Liu, J. Zhang, J.-F. Guillemoles, *Prog. Photovolt. Res. Appl.* **2022**, *30*, 581.
[82] N. E. Richey, C. de Paula, S. F. Bent, *J. Chem. Phys.* **2020**, *152*, 040902.
[83] H. Ueba, B. Gumhalter, *Dyn. Electron Transf. Process. Surf.* **2007**, *82*, 193.
[84] M. Borgwardt, S. T. Omelchenko, M. Favaro, P. Plate, C. Höhn, D. Abou-Ras, K. Schwarzburg, R. van de Krol, H. A. Atwater, N. S. Lewis, R. Eichberger, D. Friedrich, *Nat. Commun.* **2019**, *10*, 2106.
[85] G. Kresse, J. Furthmüller, *Comput. Mater. Sci.* **1996**, *6*, 15.
[86] J. P. Perdew, K. Burke, M. Ernzerhof, *Phys. Rev. Lett.* **1996**, *77*, 3865.
[87] P. E. Blöchl, *Phys. Rev. B* **1994**, *50*, 17953.
[88] G. Kresse, D. Joubert, *Phys. Rev. B* **1999**, *59*, 1758.